Strong manipulation of the valley splitting upon twisting and gating in $MoSe_2/CrI_3$ and WSe_2/CrI_3 van der Waals heterostructures

Klaus Zollner,* Paulo E. Faria Junior, and Jaroslav Fabian
Institute for Theoretical Physics, University of Regensburg, 93040 Regensburg, Germany

(Received 25 October 2022; revised 21 December 2022; accepted 21 December 2022; published 9 January 2023)

Van der Waals (vdW) heterostructures provide a rich playground to engineer electronic, spin, and optical properties of individual two-dimensional materials. We investigate the twist-angle and gate dependence of the proximity-induced exchange coupling in the monolayer transition-metal dichalcogenides (TMDCs) $MoSe_2$ and WSe_2 due to the vdW coupling to the ferromagnetic semiconductor CrI_3, from first-principles calculations. A model Hamiltonian, which captures the relevant band edges at the K/K' valleys of the proximitized TMDCs, is employed to quantify the proximity-induced exchange. Upon twisting from 0° to 30°, we find a transition of the TMDC valence band (VB) edge exchange splitting from about −2 to 2 meV, while the conduction band (CB) edge exchange splitting remains nearly unchanged at around −3 meV. For the VB of WSe_2 ($MoSe_2$) on CrI_3, the exchange coupling changes sign at around 8° (16°). We find that even at the angles with almost zero spin splittings of the VB, the real-space spin polarization profile of holes at the band edge is highly nonuniform, with alternating spin up-and spin-down orbitals. Furthermore, a giant tunability of the proximity-induced exchange coupling is provided by a transverse electric field of a few V/nm. Within our first-principles framework, we are limited to commensurate structures, and thus considered a maximum strain of 2.2% for the individual monolayers. By investigating different atomic stacking configurations of the strained supercells, we demonstrate that proximity exchange varies locally in space within experimentally realistic setups. We complement our *ab initio* results by calculating the excitonic valley splitting to provide experimentally verifiable optical signatures of the proximity exchange. Specifically, we predict that the valley splitting increases almost linearly as a function of the twist angle. Furthermore, the proximity exchange is highly tunable by gating, allowing to tailor the valley splitting in the range of 0 to 12 meV in WSe_2/CrI_3, which is equivalent to external magnetic fields of up to about 60 T. Our results highlight the important impact of the twist angle and gating when employing magnetic vdW heterostructures in experimental geometries.

DOI: 10.1103/PhysRevB.107.035112

I. INTRODUCTION

Two-dimensional (2D) materials offer a huge variety of electronic, optical, spin, magnetic, and topological properties for future applications, which can be further tailored via external knobs [1–11]. For example, straining and gating of transition-metal dichalcogenides (TMDCs) can drive structural phase transitions, accompanied by significant modifications of the aforementioned properties [12–20]. Particularly, Song *et al.* [13] demonstrated a room temperature semiconductor-metal transition in thin film $MoTe_2$, due to the 2H-1T' structural phase transition via tensile strain of only 0.2%. Furthermore, if one wants to preserve the electronic properties of a 2D monolayer, and on-demand engineer its band structure, the concept of van der Waals (vdW) heterostructures and proximity effects come into play [5,21–23]. This concept is exemplified by graphene/TMDC heterostructures, in which the characteristic Dirac and semiconductor dispersions of the individual monolayers are well preserved, but the TMDC induces a giant (meV scale) proximity spin-orbit coupling (SOC) in graphene [24,25]. In terms of applications, graphene/TMDC heterostructures can be employed for optospintronics [26,27] and spin-charge conversion [28–31], which is only possible due to the weakly coupled bilayer system, nicely demonstrating the power of vdW engineering.

Monolayer TMDCs—MoS_2, WS_2, $MoSe_2$, and WSe_2—are interesting on their own, since they are air-stable 2D semiconductors, which have a direct band gap in the optical range at the K/K' valleys of the hexagonal Brillouin zone [32–36]. External stimuli can be employed to engineer the electronic structure and the optical transitions [2,37]. For example, straining a monolayer WS_2 tunes the size of the band gap and leads to a direct-to-indirect band gap transition, as predicted by band structure calculations and observed in photoluminescence experiments [38–41]. Even though the optical excitations at K/K' valleys for unstrained monolayer TMDCs are energetically degenerate, they are helecity-sensitive—due to the lack of inversion symmetry combined with the presence of time-reversal symmetry—allowing to selectively address charge carriers at K or K' [42]. The valley is thus another potentially relevant parameter for information technology [7,43,44]. As experimentally demonstrated, valley polarizations of about 30% can be achieved in monolayer MoS_2 by optical pumping [45,46], enabling valleytronic devices [7,43,44,47,48].

*klaus.zollner@physik.uni-regensburg.de

To achieve sizable valley polarizations, giant magnetic fields need to be applied. Indeed, a magnetic field of 1 Tesla yields only 0.1–0.2 meV of Zeeman splitting [49–56]. Proximity exchange fields perform much better and can induce several meVs, without significantly altering the band structure of TMDCs [57–69]. Of particular interest are all 2D vdW heterostructures, such as the recently considered WSe_2/CrI_3 bilayers [58,65,70–73], which show a few meV of proximity exchange. Remarkably, recent experiments have demonstrated all-optical magnetization switching in such heterostructures [73]. Moreover, an asymmetric magnetic proximity interaction has been recently observed in $MoSe_2/CrBr_3$ van der Waals heterostructures [74]. Nevertheless, most of these investigations have not considered the consequence of one important control parameter, which is the twist angle.

Only recently the relative twist angle between the monolayers has been recognized as a crucial degree of freedom. The most prominent examples are twisted bilayer and trilayer graphene, exhibiting magnetism and superconductivity due to strong correlations [75–99]. Other platforms for correlated physics are offered by twisted TMDCs [100–102] and twisted CrI_3 mono- and bilayers [103,104]. Regarding proximity effects, a recent study shows the sensitivity of the spin polarization, magnetic anisotropy, and Dzyaloshinskii-Moriya interaction on the twist angle in graphene/2H-VSeTe heterostructures [105]. Similarly, theoretical [106–112] and experimental [113] studies show that the strength of proximity SOC in graphene/TMDC and the proximity exchange in graphene/$Cr_2Ge_2Te_6$ [114] heterostructures can be tuned by the twist angle.

In our previous work [72] on TMDC/CrI_3 bilayers, we have only considered two twist angles, 0° and 30°, predicting a significant (meV scale) proximity exchange, with different sign for the TMDC valence band (VB) edge spin splitting at the two twist angles. No detailed study of the effect has been done for intermediate twist angles to see if the sign change is systematic or accidental. Another important question relates to the proximity exchange of the conduction band (CB): does the direction of the proximity exchange remain independent of the twist angle, as suggested by the 0° and 30° predictions? What is the variation of the magnitude of the proximity exchange as a function of the twist angle? Could there be a scenario such as predicted for graphene/$Cr_2Ge_2Te_6$ [114] that the effective proximity exchange becomes antiferromagnetic at an intermediate angle? What are the real-space spin-polarization profiles of the conduction and valence electrons in the TMDCs for different twist angles? In the present study, we systematically address these questions.

Recent band structure investigations of WSe_2/CrI_3 heterostructures by Ge *et al.* [115] revealed a relative valley splitting enhancement of about 1000% by twisting, in good agreement with Ref. [72]. They have shown that mainly the TMDC VB splitting is responsible for the massive twist tunability of the valley splitting. In addition they also found a reversal of the VB splitting and related valley splitting upon twisting, but did not analyze this fact. Overall, the tunability of the valley splitting is attributed to the magnetic proximity effect and related to the enhancement of the Cr magnetic moments upon twisting. However, Ge *et al.* [115] considered just four twist angles and rather large strains of up to 5.5%, with respect to the lattice constants determined from density functional theory (DFT), which significantly alters both monolayer dispersions and CrI_3 magnetic properties [39,116]. In addition, an electric field dependence was performed only for one specific twist angle of 16.1°.

Here, we systematically investigate the twist-angle and electric-field dependence of the proximity-induced exchange coupling in $MoSe_2/CrI_3$ and WSe_2/CrI_3 bilayers, from first principles. We consider seven different angles between 0° and 30° with a maximum strain—needed for commensurability of the unit cells—of about 2.2% applied to the monolayers when employing experimentally determined lattice constants. Within the heterostructures the TMDCs preserve their characteristic dispersion, while the magnetic insulator substrate provides proximity exchange, splitting the relevant TMDC VB and CB edges (in the absence of SOC, see below) at K/K' valleys. Depending on the relative twist angle the band edge splittings can be markedly different, and even the spin ordering can be reversed. In particular, when twisting from 0° to 30°, the TMDC CB edge splitting remains nearly unchanged at around −3 meV. In contrast, there is a smooth transition of the TMDC VB edge spin splitting from about −2 to 2 meV (the spin ordering changes). The finding about the reversal of the spin ordering is consistent with Ref. [72], but here we additionally find that it happens in an almost linear fashion upon twisting, and we identify the twist angles at which the transition happens: about 8° (16°) for WSe_2 ($MoSe_2$). The origin of this reversal is traced back to the twist-angle dependent backfolding of the TMDC K/K' valleys into the CrI_3 Brillouin zone. By investigating different atomic stacking configurations of the strained supercells, we show that proximity exchange varies locally in space within experimentally realistic heterostructures.

Furthermore, we reveal a rather high tunability of the proximity-induced exchange coupling by applying a transverse electric field of a few V/nm across all the twisted WSe_2/CrI_3 heterostructures. In Ref. [72], the electric field tunability was investigated for the 0° structure only. We also introduce a minimal model Hamiltonian to describe the twist- and gate-tunable proximity effects in the TMDCs due to CrI_3. The Hamiltonian together with the fitted parameters provide an effective description for the TMDC band edge physics at K/K' valleys, which is relevant for calculating magneto-optical Kerr effect [117,118], absorption spectra [72,119,120], or coupled spin Hall and valley Hall effects [42]. Finally, we give specific predictions for experimentally verifiable optical signatures of the proximity exchange effects, by calculating the excitonic absorption spectra employing the Bethe-Salpeter equation. In addition to 0° and 30° angles [72], we provide the full twist-angle and electric-field dependence of the valley splitting. We find a rather high tunability of the valley splitting of the first intralayer exciton peak, ranging from 0 to 12 meV by gating and twisting in WSe_2/CrI_3 bilayers, equivalent to external magnetic fields of up to about 60 T.

The paper is organized as follows. In Sec. II, we first address the structural setup and summarize the calculation details for obtaining the electronic structures of the twisted TMDC/CrI_3 bilayers. In Sec. III, we introduce the model Hamiltonian that captures the relevant band edges at K/K' valleys of the proximitized TMDCs, which are used to fit the

TABLE I. Structural information for the TMDC/CrI_3 heterostructures. We list the twist angle ϑ between the layers, the number of atoms (NoA) in the heterostructure supercell, the number n_k for the k-point sampling, the lattice constants and biaxial strains ε applied to the TMDCs and CrI_3, the calculated dipoles and the relaxed interlayer distances d_{int} of the $MoSe_2$ (WSe_2) structures.

ϑ (deg)	NoA	n_k	a_{TMDC} (Å)	$\varepsilon_{\text{TMDC}}$ (%)	a_{CrI3} (Å)	$\varepsilon_{\text{CrI3}}$ (%)	dipole (debye)	d_{int} (Å)
0.0000	20	30	3.3608	2.21	6.7215	−2.12	0.0507 (0.1082)	3.5467 (3.5000)
8.2132	243	9	3.3400	1.58	6.7472	−1.75	0.0322 (0.5475)	3.5888 (3.5661)
10.1583	149	12	3.2880	0	6.9189	0.76	0.3590 (0.6993)	3.5858 (3.5749)
16.1021	63	24	3.2880	0	6.8444	−0.33	0.0881 (0.2474)	3.5930 (3.5490)
21.7868	140	12	3.3610	2.22	6.7189	−2.16	−0.0725 (0.2432)	3.5666 (3.5499)
25.2850	183	9	3.3350	1.43	6.7604	−1.55	0.0033 (0.4402)	3.5885 (3.5627)
30.0000	243	9	3.3400	1.58	6.7492	−1.72	−0.0347 (0.5360)	3.5837 (3.5640)

first-principles results. In Sec. IV, we show and discuss exemplary calculated electronic structures, along with the model Hamiltonian fits. The twist-angle and gate dependence of the proximity-induced exchange couplings is also addressed. In Sec. V, we show and discuss the twist-angle and electric-field tunability of the valley splitting, as calculated from the absorption spectra employing the Bethe-Salpeter equation. Finally, in Sec. VI, we conclude the manuscript.

II. GEOMETRY SETUP & COMPUTATIONAL DETAILS

The twisted $MoSe_2/CrI_3$ and WSe_2/CrI_3 heterostructures for the DFT calculations are set up with the ATOMIC SIMULATION ENVIRONMENT (ASE) [121] and the CELLMATCH code [122], implementing the coincidence lattice method [123,124]. Monolayers of TMDCs and CrI_3 are based on hexagonal unit cells, with lattice constants of $a = 3.288$ Å ($MoSe_2$), $a = 3.282$ Å (WSe_2), and $a = 6.867$ Å (CrI_3) [125–127], which need to be strained in the twisted heterostructures, in order to form commensurate supercells for periodic DFT calculations. Since $MoSe_2$ and WSe_2 have nearly the same lattice constant, we set them as equal in the following. In Table I, we summarize the main structural information for the twist angles we consider. All our heterostructures have C_3 symmetry. In Fig. S1 [128], we show top views of all employed supercell geometries. In total, we investigate seven different angles between 0° and 30°. Especially these angles are suitable for DFT calculations, since strain applied to the monolayers is at maximum 2.2%. We already know that biaxial strain strongly influences the band gap, spin-orbit splittings and spin-valley properties of monolayer TMDCs [39,56], as well as the band gap of CrI_3 [116], therefore we keep the strain as small as possible. In addition, the number of atoms is kept below 250. Otherwise, also other angles could be investigated, but beyond reasonable strain limits and above a computationally feasible number of atoms in the structure.

The electronic structure calculations and structural relaxation of the TMDC/CrI_3 heterostructures are performed by DFT [129] with QUANTUM ESPRESSO [130,131]. Self-consistent calculations are carried out with a k-point sampling of $n_k \times n_k \times 1$. The number n_k is listed in Table I for all twist angles and depends on the number of atoms in the heterostructure. In addition, n_k is limited by our computational power. Nevertheless, for large supercells the heterostructure Brillouin zone is small and only a few k points are necessary to get converged results.

We perform open shell calculations that provide the spin-polarized ground state of the CrI_3 monolayer. A Hubbard parameter of $U = 3.0$ eV is used for Cr d orbitals [72,132]. We use an energy cutoff for charge density of 520 Ry and the kinetic energy cutoff for wave functions is 65 Ry for the scalar relativistic pseudopotentials with the projector augmented wave method [133] with the Perdew-Burke-Ernzerhof exchange correlation functional [134]. SOC is neglected, since we are mainly interested in the twist-angle dependence of the proximity-induced exchange coupling. Moreover, we have already demonstrated that SOC and proximity exchange are rather independent in the investigated bilayers [72]. For the relaxation of the heterostructures, we add DFT-D2 vdW corrections [135–137] and use quasi-Newton algorithm based on trust radius procedure. Dipole corrections [138] are also included to get correct band offsets and internal electric fields. In order to simulate quasi-2D systems, we add a vacuum of about 24 Å to avoid interactions between periodic images in our slab geometry. For proper interlayer distances, we allow the atoms of the TMDCs, as well as the Cr atoms of the CrI_3, to relax their z coordinates, while the I atoms are allowed to move freely, because they form a distorted octahedral surrounding around the Cr atoms [139]. Relaxation is performed until every component of each force is reduced below 10^{-3} [Ry/a_0], where a_0 is the Bohr radius.

After relaxation, we calculate the mean interlayer distances, d_{int}, from the z coordinates of interfacial Se and I atoms. The interlayer distances are nearly independent of the twist angle, about 3.55 Å, and are listed in Table I. In Fig. 1, we show the general structural setup of our TMDC/CrI_3 heterostructures, where the TMDC resides above CrI_3, with the magnetization $\boldsymbol{M}$ along z direction specifying the spin quantization axis (spin up $= z$, spin down $= -z$). When we apply the transverse electric field (modeled by a zigzag potential), a positive field also points along z direction.

III. MODEL HAMILTONIAN

We want to describe proximity exchange effects in the monolayer TMDCs that are due to the magnetic insulator substrate CrI_3. Similar to our recent work [72], we employ a minimal model Hamiltonian to describe the band edges of the

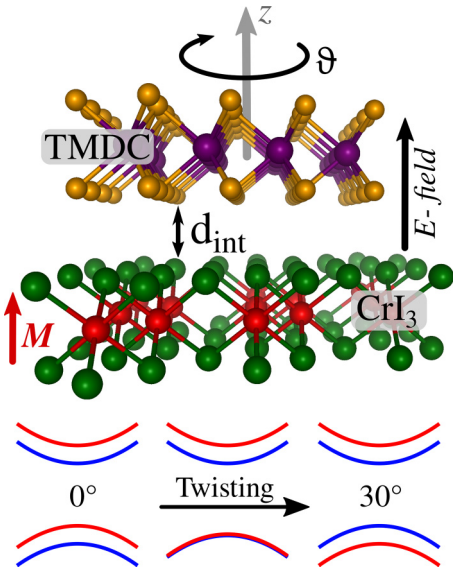

FIG. 1. 3D view of a TMDC ($MoSe_2$ or WSe_2) on CrI_3, where we define the interlayer distance, d_{int}. We twist the TMDC by an angle ϑ around the z axis, with respect to the magnetic semiconductor CrI_3, with magnetization $\boldsymbol{M}$ along the z direction. The twist-angle evolution of the proximitized TMDC band edges are sketched. Red bands are polarized spin up, while blue bands are polarized spin down. By twisting from 0° to 30°, the TMDC VB edge splitting, which is due to proximity exchange, first vanishes and then reverses sign.

TMDC close to K and K' valleys, in the presence of proximity exchange

$$\mathcal{H} = \mathcal{H}_0 + \mathcal{H}_\Delta + \mathcal{H}_{\rm ex}, \tag{1}$$

$$\mathcal{H}_0 = \hbar v_{\rm F} s_0 \otimes (\tau\sigma_x k_x + \sigma_y k_y), \tag{2}$$

$$\mathcal{H}_\Delta = \frac{\Delta}{2} s_0 \otimes \sigma_z, \tag{3}$$

$$\mathcal{H}_{\rm ex} = -s_z \otimes (B_{\rm c}\sigma_+ + B_{\rm v}\sigma_-). \tag{4}$$

The valley index is $\tau = \pm 1$ for K/K' point and $v_{\rm F}$ is the Fermi velocity. The Cartesian components k_x and k_y of the electron wave vector are measured from K/K'. The pseudospin Pauli matrices are $\sigma_{\rm i}$ acting on the [conduction band (CB), valence band (VB)] subspace and spin Pauli matrices are $s_{\rm i}$ acting on the $(\uparrow, \downarrow)$ subspace, with ${\rm i} = \{0, x, y, z\}$. The parameter Δ denotes the orbital gap of the spectrum. For short notation, we introduce $\sigma_\pm = \frac{1}{2}(\sigma_0 \pm \sigma_z)$. With a magnetic substrate layer, proximity exchange coupling will split the TMDC CB edge by $2B_{\rm c}$ and the VB edge by $2B_{\rm v}$. The four basis states we use are $|\Psi_{\rm CB}, \uparrow\rangle$, $|\Psi^\tau_{\rm VB}, \uparrow\rangle$, $|\Psi_{\rm CB}, \downarrow\rangle$, and $|\Psi^\tau_{\rm VB}, \downarrow\rangle$. The wave functions are $|\Psi_{\rm CB}\rangle = |d_{z^2}\rangle$ and $|\Psi^\tau_{\rm VB}\rangle = \frac{1}{\sqrt{2}}(|d_{x^2-y^2}\rangle + {\rm i}\tau|d_{xy}\rangle)$, corresponding to CB and VB at K/K' [32].

IV. TWIST- AND GATE-TUNABLE PROXIMITY EXCHANGE

A. Twist angle dependence

In Fig. 2(a), we show the DFT-calculated band structure of the $MoSe_2/CrI_3$ heterostructure for a twist angle of 0°. The band edges of the TMDC can be nicely recognized at the K point at about −0.5 and 0.8 eV with respect to the Fermi level. The states ranging from about 0 to 0.5 eV are spin polarized in-gap states that originate from the CrI_3 layer. Therefore the heterostructure forms a type-II band alignment with a bandgap ΔE of about 0.5 eV. In our heterostructures, small charge transfer is present between the monolayers, leading to a finite intrinsic electric (dipole) field. The dipole of the heterostructure, which controls the band alignment and ΔE, depends on the twist angle, as summarized in Table II. However, we

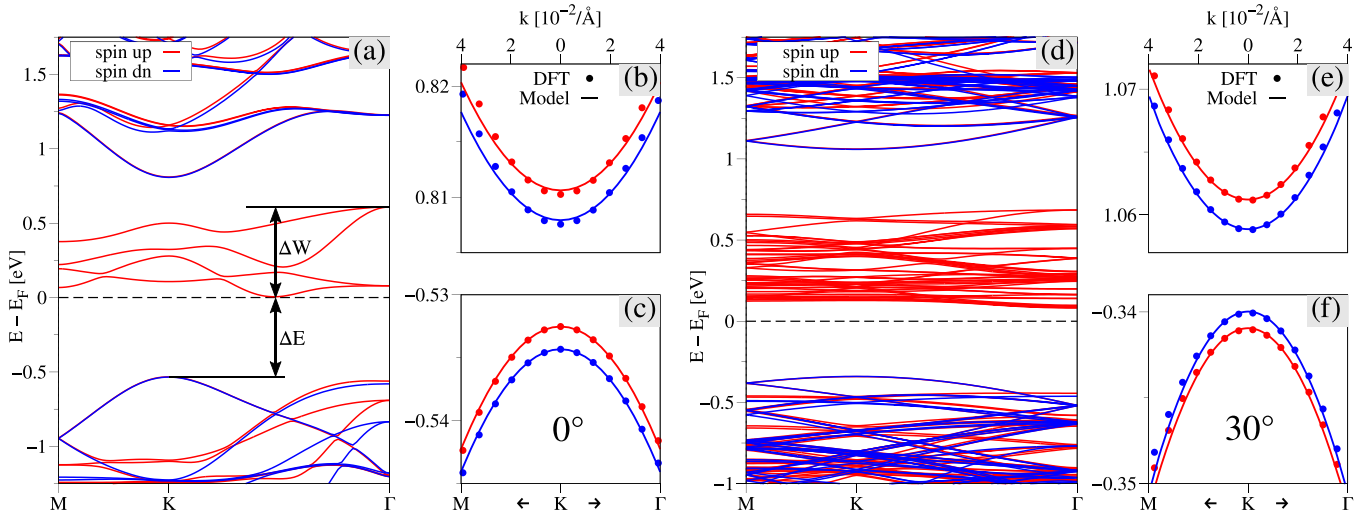

FIG. 2. (a) DFT-calculated band structure of the $MoSe_2/CrI_3$ heterostructure for a twist angle of 0° along the high-symmetry path M-K-Γ. Bands in red are spin up, while bands in blue are spin down. We define the heterostructure band gap ΔE, between the TMDC VB edge at K, and the minimum of spin polarized CrI_3 in-gap states. We also define the bandwidth ΔW of the in-gap states. (b) Zoom to the $MoSe_2$ CB edge near the K point, showing proximity exchange split bands. Symbols are DFT data and solid lines are the fitted model Hamiltonian results. (c) Same as (b), but for the VB edge. [(d)–(f)] Same as [(a)–(c)], but for a twist angle of 30°. Comparing (c) and (f), the spin ordering of bands is reversed.

TABLE II. Fit parameters of Hamiltonian $\mathcal{H}$ for the TMDC/CrI_3 heterostructures for different twist angles. We summarize the Fermi velocity v_F, the orbital gap Δ, proximity exchange parameters B_c and B_v, the heterostructure band gap ΔE, and the CrI_3 in-gap states bandwidth ΔW, as defined in Fig. 2(a).

	ϑ (deg)	v_F ($\times 10^5$ m/s)	Δ (eV)	B_c (meV)	B_v (meV)	ΔE (eV)	ΔW (eV)
$MoSe_2$	0.0000	4.358	1.343	−1.343	−0.901	0.538	0.603
	8.2132	4.631	1.403	−1.070	−0.262	0.432	0.601
	10.1583	4.626	1.555	−1.427	−0.365	0.330	0.485
	16.1021	4.622	1.556	−1.332	−0.012	0.337	0.535
	21.7868	4.575	1.340	−1.253	0.213	0.463	0.617
	25.2850	4.048	1.415	−1.221	0.415	0.417	0.587
	30.0000	4.622	1.401	−1.176	0.484	0.422	0.603
WSe_2	0.0000	5.873	1.403	−1.460	−0.918	0.377	0.600
	8.2132	5.954	1.479	−1.175	−0.020	0.255	0.601
	10.1583	6.093	1.674	−1.553	0.099	0.165	0.484
	16.1021	6.084	1.674	−1.500	0.705	0.178	0.535
	21.7868	5.839	1.403	−1.318	0.894	0.291	0.615
	25.2850	5.216	1.495	−1.290	1.415	0.248	0.587
	30.0000	5.940	1.477	−1.226	1.525	0.251	0.604

believe that the strain that is applied to the monolayers has the most significant impact on the band alignment, as previous studies of graphene-based heterostructures suggest [108,114]. Therefore the intrinsic band alignment that should be present in experiments can be read off from the 16.1° structure, with marginally strained monolayers (0.33% of strain). In addition, the CrI_3 in-gap states bandwidth ΔW depends on the lattice constant used in the heterostructure. Compressive (tensile) strain increases (decreases) ΔW. Finally, also the TMDC band gap Δ depends on the lattice constant and is strain tunable [39]. However, the 0° and 30° structures have rather similar strain, and still the proximity exchange is opposite for the VB; this strongly suggests that the variation of the proximity exchange with the twist angle is not much affected by the modest strain we have in the supercells.

In Figs. 2(b) and 2(c), we show the zooms to the $MoSe_2$ band edges near the K point for the 0° structure. The bands experience proximity-induced exchange splitting of about 2 meV. The spin ordering is the same for CB and VB, with the spin down band lower in energy. The fit parameters from Table II nicely reproduce the TMDC band edges. In Figs. 2(d)–2(f), we summarize the results for the $MoSe_2/CrI_3$ heterostructure for a twist angle of 30°. Overall, the band structure features remain the same, but with many more bands due to the larger supercell size compared to the 0° structure. Looking at the relevant TMDC band edges, proximity exchange splitting is still present, but the VB spin ordering is *reversed* compared to the 0° case. The CB proximity exchange remains the same. Below and in Ref. [128], we further elaborate on the origin of this reversal.

In Fig. 3, we summarize the twist-angle dependence of the proximity exchange parameters, B_c and B_v, as listed in Table II for the $MoSe_2$ and WSe_2 heterostructures. We find that the twist angle barely influences the CB proximity exchange parameter B_c, being fixed at around −1.2 meV. In contrast, the VB proximity exchange parameter, B_v, is negative for 0°, *vanishes and reverses sign* at about 16° (8°) for $MoSe_2$ (WSe_2), and is positive for a twist angle of 30°. The atomic arrangement (stacking) of the monolayers, for a fixed twist angle, can also influence proximity exchange [71,72], see Ref. [128] for more detailes. Apparently, for the different twist angles, we have chosen the stackings such that B_c shows a kink around 8°.

For completeness, in Ref. [128], we investigate different atomic stacking configurations and also briefly address the twist angles between 30° to 60°. Overall, we find that in large supercells the stacking only marginally influences proximity exchange couplings, while in small supercells—such as the 0° structure with only 20 atoms—the VB edge splitting can be tuned in sign and magnitude by the atomic arrangement, see also Fig. 4. We believe that an averaging effect takes place in larger supercell geometries, where a lot of atoms are involved in forming the TMDC band edge states, which can locally pick up different exchange fields, but globally lead to the same band edge splitting. In other words, experimentally the proximity exchange will vary locally in space across the heterostructure.

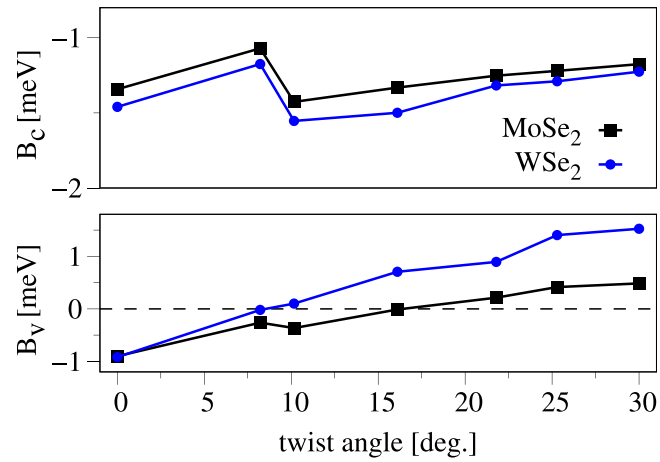

FIG. 3. Calculated twist-angle dependence of the proximity exchange couplings B_c and B_v for the $MoSe_2/CrI_3$ and WSe_2/CrI_3 heterostructures.

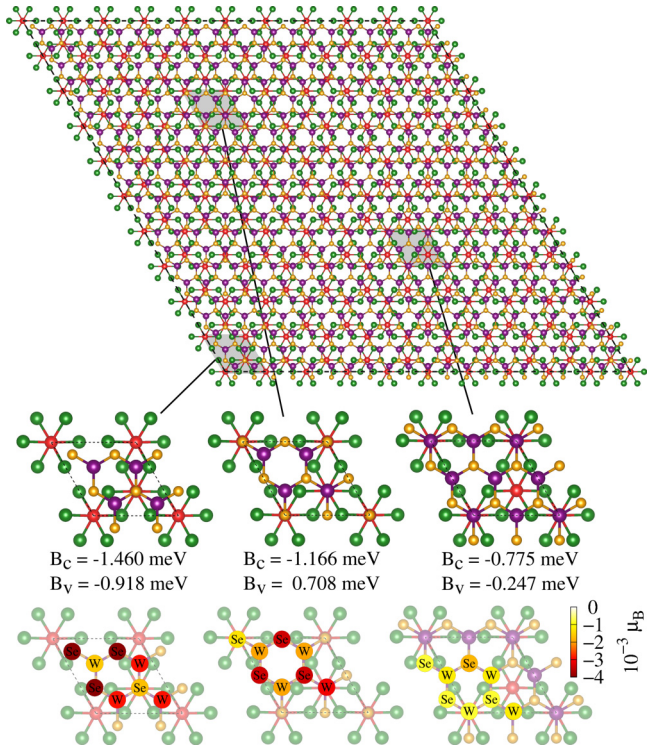

FIG. 4. (Top) An experimentally realistic 0° WSe_2/CrI_3 heterostructure (2123 atoms), where we consider a 21 × 21 supercell of WSe_2 on a 10 × 10 supercell of CrI_3, corresponding to strains of 0% and 0.5%. (Middle) Different high-symmetry stackings of the 0° strained heterostructure are locally indicated, with their corresponding proximity exchange parameters B_c and B_v. (Bottom) Calculated proximity-induced local magnetic moments (colored spheres) of the interfacial Se and W atoms for the different stackings.

Such a local variation can be seen in Fig. 4 (Fig. S2), where we also show the proximity-induced local magnetic moments of interfacial Se and W atoms of different 0° stacking configurations (of all investigated heterostructures). We find that the induced magnetic moments depend sensitively on the stacking and correlate with the proximity exchange parameters B_c and B_v. With high-resolution vector magnetometry and gradiometry, based on nitrogen-vacancy centers in diamond [140–142], one can potentially resolve the demonstrated local variations of proximity exchange.

In Figs. 4 and S19, we explicitly map different high-symmetry stackings of our strained 0° structure to an experimentally more realistic setup, further confirming the local variation of proximity exchange. In fact, the proximity exchange parameter B_c varies by a factor of 2 among the investigated stackings, while the parameter B_v can be even reversed in sign and magnitude. However, one has to relate this with experimental limitations. Even though there can be local variations of proximity exchange, typical photoluminescence techniques are not capable of addressing only a specific stacking. Then, even for the 0° case, an ensemble of stackings will be probed, thus leading to an average proximity exchange. Based on the findings for different stackings, the average exchange splittings follow the same predictions as we provide in Fig. 3 (VB and CB splittings negative for 0°). Moreover, twisting from 30° to 60° leads to similar proximity exchange couplings—apart from differences in magnitude owed to the atomic stacking—as twisting from 30° to 0°.

As mentioned above, the strain is a byproduct of our structural setup, leading to nontrivial influences on band gaps and magnetic properties of our monolayers [39,116]. In Ref. [128], we also investigate the influence of the strain distribution for the WSe_2/CrI_3 structure with 0° twist angle. We find that the exchange parameters can be changed by at maximum ±20% by tuning the strain, but their signs and the order of magnitude remains. In other words, the presented results are representative for experimental conditions (no or weak strain). Based on the findings for 0°, one can expect a similar strain dependence for the other investigated twist angles, where strain is similar or smaller compared to 0°, see Table I. Especially for the 10.2° and 16.1° structures, where strain is small, we believe our calculations provide a close correspondence to experimental results.

Regarding experiments, one can expect similar results for few layer CrI_3, including even and odd number of layers. In Ref. [72], we have shown that the proximity exchange coupling is restricted to interfacial layers, i.e., mainly the topmost CrI_3 layer influences the TMDC. In particular, we have shown that proximity exchange for TMDC on bilayer CrI_3 in ferro- and antiferromagnetic configuration is essentially unchanged. Of course, the sign of the proximity effect does depend on the magnetization direction of the interfacial CrI_3 layer, but not the magnitude.

B. Electric field tunability

In experimental geometries, gating is a useful tool to further control and tailor the proximity exchange coupling in TMDC/magnetic-semiconductor heterostructures. In the following, we consider the experimentally relevant WSe_2/CrI_3 heterostructure [58,65,70] and perform a gate scan, in the range of ±2 V/nm, for all twist angles. The electric-field and twist-angle dependence of the proximity exchange parameters B_c and B_v is summarized in Fig. 5, while the full fit results are summarized in Table S2 [128]. For all angles and electric fields we consider, the CB proximity exchange parameter, B_c, stays negative and within the limits of about −0.5 to −2.5 meV. In contrast, the VB proximity exchange parameter B_v can be even stronger controlled by the electric field and the twist angle. As already mentioned, we find a crossover from positive to negative values at around 8° twist angle for WSe_2. Furthermore, the applied field allows to tune B_v in a wide range of values. Considering all angles, the tunability is giant and within the limits of about −1.5 to 4 meV.

C. Reversal of the valence band proximity exchange splitting

The reversal of the TMDC VB edge splitting upon twisting is one of the most interesting findings, see Fig. 3. A similar reversal of the proximity-induced exchange coupling has been recently found in graphene/$Cr_2Ge_2Te_6$ bilayers when twisting from 0° to 30° [114]. The reversal was attributed to the different coupling of C orbitals to the spin up and spin down band manifolds of the magnetic substrate for the different twist angles. What is the mechanism for the investigated TMDC/CrI_3

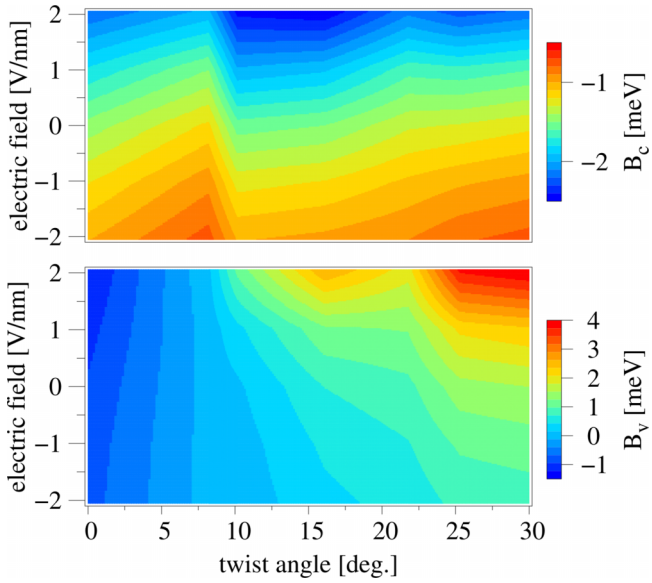

FIG. 5. Calculated electric-field and twist-angle dependence of the proximity-induced exchange parameters B_c (top) and B_v (bottom) for the WSe_2/CrI_3 heterostructure, interpolated from Table S2.

bilayers? For this purpose, we analyze the twisted WSe_2/CrI_3 heterostructures in more detail. In particular, we look at the three most relevant twist angles, namely, 0°, 8.2°, and 30°, corresponding to the cases when the WSe_2 VB edge proximity exchange splittings are negative, almost zero, and positive. A similar analysis should hold for $MoSe_2$, but the splitting vanishes at a different twist angle. In the following, we want to address the main points, while a more detailed discussion is given in Ref. [128].

To gain information about the proximity-induced exchange coupling, we look a the TMDC band edge spin polarizations in real space. Considering only TMDC CB edge states near the K point, the calculated spin polarization is negative, independent of the twist angle and in agreement with the band edge dispersion, predominantly formed by W d_{z^2} orbitals, and localized only on the WSe_2 layer (see Fig. 6). In other words, the low-energy TMDC CB edge states, which are spin-split due to proximity exchange, do not contain a spin polarization from the CrI_3 layer. Indeed, mainly in the spin down channel the high-energy TMDC and CrI_3 bands are coupled, as one can see in the projected band structures for the three twist angles (see Figs. S3, S7, and S10). Considering second-order perturbation theory, the dominant coupling between spin down high-energy levels can repel the TMDC spin down band edge states to lower energies compared to the spin up ones, consistent with the observed splittings in Figs. 2(b) and 2(e). Additionally considering the coupling to CrI_3 spin up in-gap states leads to the same conclusion.

The explanation for the VB edge is a bit more involved. In Fig. 6, we also show the calculated TMDC VB edge spin polarizations for 0°, 8.2°, and 30°. In the case of 0°, the VB edge splitting is negative [the dispersion is sketched in Fig. 6(a)]. This leads to the positive spin polarization we can see in Fig. 6(a), which is spread uniformly across the TMDC and

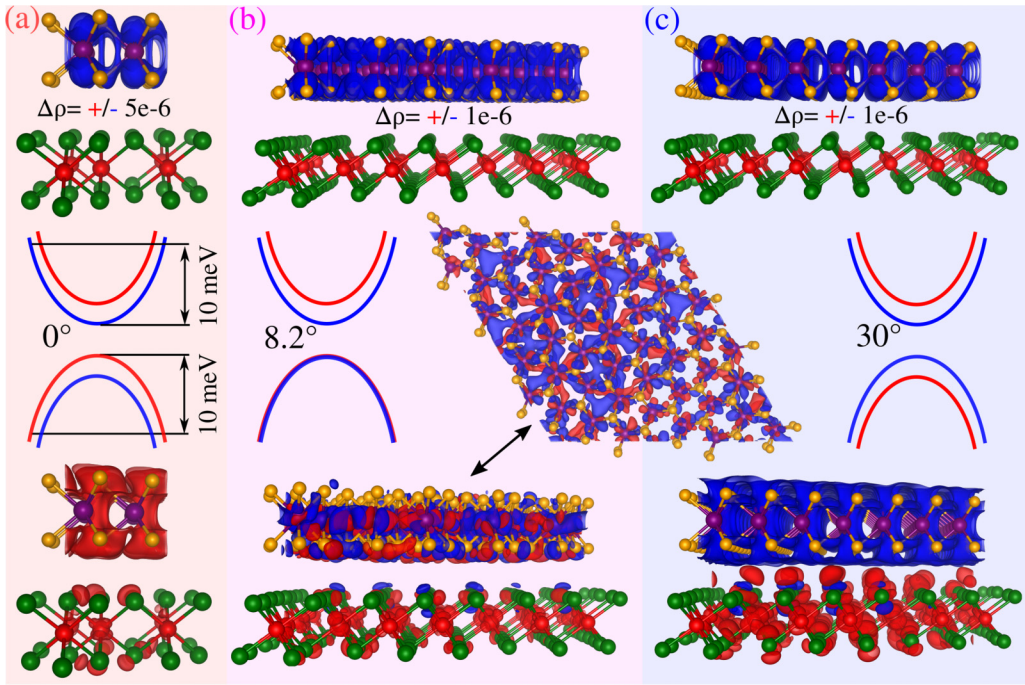

FIG. 6. Calculated real-space TMDC band edge spin polarizations, $\Delta\rho = \rho_\uparrow - \rho_\downarrow$, for the twisted WSe_2/CrI_3 heterostructures. The background color is used to group the subfigures for the three twist angles (a) 0°, (b) 8.2°, and (c) 30°. (a) (Middle) Sketch of the proximitized TMDC band edges for 0°, where we indicate the energy windows from which we calculate the spin densities $\rho_{\uparrow/\downarrow}$.(Top/bottom) Calculated band edge spin polarization, taking into account only CB/VB states. The color red (blue) corresponds to $\Delta\rho > 0$ ($\Delta\rho < 0$). The isosurfaces correspond to isovalues (units $Å^{-3}$) as indicated. (b) The same as (a), but for 8.2°. For the VB, we also show a top view, with removed CrI_3 layer, to show the nonuniform spin polarization on WSe_2. (c) The same as (a), but for 30°.

predominantly formed by W $d_{xy} + d_{x^2-y^2}$ and Se p orbitals. In addition, Cr $d_{zx} + d_{zy}$ and I $p_x + p_y$ orbitals contribute to the TMDC VB edge spin polarization. For the 30° case, we find the opposite and a uniform negative band edge spin polarization on the TMDC, see Fig. 6(c), again in agreement with the dispersion. For 8.2°, the VB edge splitting almost vanishes and we find a highly nonuniform spin polarization, see Fig. 6(b), with a multipole character around the W atoms. On average, the spin polarization is zero and therefore the band splitting is absent, but this does not rule out the complex spin structure we find. In fact, since the proximity exchange can sensitively depend on the stacking, as we have shown especially for the 0° supercell, one can expect local variations of the band edge spin polarizations also in experimentally realistic setups of the other twist angles. Analyzing the TMDC VB states in more detail, there is apparently a delicate balance between the coupling to CrI_3 spin polarized in-gap and VB states. What is different is the backfolding of the TMDC K point into the Brillouin zone of CrI_3 for different twist angles. For example, for 0° the TMDC K point folds back near the CrI_3 K point, while at 30° it folds back near the Γ point, see Fig. S5. Since the interlayer coupling is different at different k points, and also different CrI_3 band manifolds and orbitals play a role, this could indeed lead to the reversal of the TMDC VB edge splitting.

V. TWIST- AND GATE-TUNABLE VALLEY SPLITTING

In order to provide insight into the optical signatures of the proximity exchange, we evaluate the valley splitting, i.e., the energy separation between the absorption peaks with opposite circular polarization (σ^+ and σ^-). Combining the proximity exchange parameters, B_c and B_v, from Table S2 [128], with the intrinsic SOC parameters for $MoSe_2$ and WSe_2 monolayers (see, for example, Ref. [39]), we can provide valuable insights regarding the twist-angle and electric-field dependence of the valley splitting. Besides the Hamiltonian terms given in Eq. (1), the SOC term reads

$$H_{\text{soc}} = \tau s_z \otimes (\lambda_c \sigma_+ + \lambda_v \sigma_-), \tag{5}$$

with parameters $\lambda_v = 94.56$ meV and $\lambda_c = -9.647$ meV for $MoSe_2$, and $\lambda_v = 241.79$ meV and $\lambda_c = 13.9$ meV for WSe_2, taken from Ref. [72].

To incorporate excitonic effects and calculate the absorption spectra, we apply the robust formalism of the effective Bethe-Salpether equation with the electron-hole Coulomb interaction mediated by the Rytova-Keldysh potential, similar to Refs. [72,120]. From the calculated absorption, we can extract the valley splitting, i.e., the energy difference between the first A exciton peaks at K and K' (with opposite circular polarization). For the excitonic calculations, the BSE is solved numerically using 101 × 101 k points in a square region with sides ranging from −0.5 to 0.5 Å^{-1}, thus leading to a k-point spacing of $\Delta k = 10^{-2}$ Å^{-1} along each direction. Additionally, the Coulomb potential is averaged in a submesh of 101 × 101 points covering an area of Δk^2 around each k point. The screening length used in the calculations is $r_0 = 51$ (45) Å for $MoSe_2$ (WSe_2), from Ref. [143], and the dielectric constant for CrI_3 is taken as $\epsilon = 1.8$, from Ref. [144].

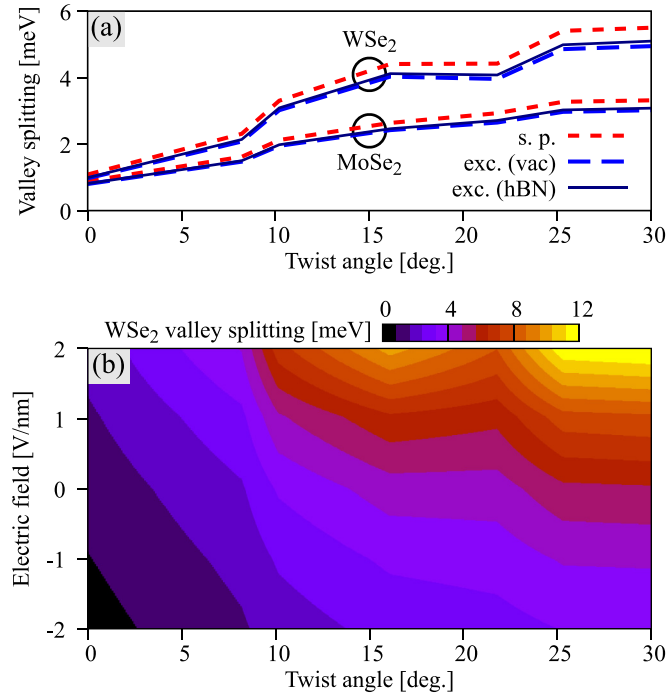

FIG. 7. (a) Valley splitting for the $MoSe_2/CrI_3$ and WSe_2/CrI_3 bilayers calculated from the single-particle (abbreviated by s.p., short dashed lines), and from the excitonic absorption (abbreviated as exc.) considering the region above the TMDC to be vacuum (long dashed lines) or hexagonal boron nitride (solid lines). The single-particle values follow nicely the excitonic calculations. (b) Valley splitting for the WSe_2/CrI_3 bilayer as function of the twist angle (x axis) and applied electric field (y axis) using the single-particle values, calculated via Eq. (6).

In the single-particle limit, i.e., where no excitonic effects are taken into account, the valley splitting can be obtained analytically by solving the Hamiltonians (1) and (5) and is given by

$$\begin{aligned} \text{VS} &= (E_{c\uparrow,\text{K}} - E_{v\uparrow,\text{K}}) - (E_{c\downarrow,\text{-K}} - E_{v\downarrow,\text{-K}}) \\ &= -2(B_c - B_v). \end{aligned} \tag{6}$$

In Fig. 7(a), we reveal the behavior of the valley splitting as a function of the twist angle for $MoSe_2/CrI_3$ and WSe_2/CrI_3. For both cases, the valley splitting increases as the twist angle gets larger, almost in a linear fashion. The role of excitonic effects due to different environments on top of the TMDC is also explored: air/vacuum with $\varepsilon = 1$ (long dashed lines) and hexagonal boron nitride with $\varepsilon = 4.5$ [145–147] (solid lines). The single-particle values (short dashed lines), obtained from Eq. (6), are also shown and follow closely the trends of the excitonic valley splitting extracted from the absorption spectra (shown in the Supplemental Material [128]), suggesting that it is possible to grasp valuable insight into the valley splitting just by knowing the exchange parameters B_c and B_v extracted from DFT calculations. Our results reveal that the twist-angle is a crucial parameter for the assembly of TMDC/ferromagnetic-semiconductor vdW heterostructures and, particularly, it has a sizable impact on the magnitude of the valley splitting.

To highlight the extraordinary tunability of the valley splitting by the combined effect of the twist angle and gating, we show in Fig. 7(b) a complete color map for the WSe_2/CrI_3 system, using the single-particle valley splitting expression of Eq. (6). On the bottom left corner of the figure, the valley splitting nearly vanishes for 0° twist angle and ~ -2 V/nm, whereas on the top right corner, the valley splitting reaches very large values of approximately 12 meV for 30° and $\sim$2 V/nm. For a fixed twist angle, the dependence of the valley splitting is almost linear, in agreement with our previous calculations [72] and experimentally demonstrated in $MoSe_2/CrBr_3$ samples [68].

VI. SUMMARY

We have shown that, by employing first-principles calculations on large supercells, one can tailor the proximity exchange coupling in TMDC/CrI_3 bilayers by twisting and gating. The previously observed reversal of the proximity exchange is demonstrated to result from a systematic, essentially linear dependence of the exchange in the VB on the twist angle. We do not find any significant variation in the CB.

Analyzing the real-space spin-resolved electronic density for the band edges, we find that the CB electrons exhibit a uniform spatial spin polarization for all the investigated twist angles. In contrast, the hole spin polarization undergoes remarkable transformations as going from 0° to 30°. While at the two limit angles the spin polarizations are highly uniform, albeit opposite (corresponding to the opposite spin splittings), at the twist angles where the spin splitting reverses sign the spin polarization is highly nonuniform, alternating between spin up and spin down orbitals, arising from a subtle balance between orbital- and spin-resolved hybridization of the TMDC and CrI_3 orbitals. By comparing different stacking configurations, we have also demonstrated that the induced magnetic moments, proximity exchange, and the spin polarizations can vary locally in space within experimentally realistic setups.

Further substantial tunability of the band edge splittings is provided by a transverse electric field of a few V/nm. A low-energy model Hamiltonian, with fitted parameters that nicely reproduce the relevant DFT-calculated band edges of the proximitized TMDCs, has been employed to reveal the experimentally verifiable signatures of the CrI_3 exchange field on the valley splitting of the first TMDC exciton peak. Particularly, we predict that the valley splitting increases linearly with respect to the twist angle. Furthermore, in WSe_2/CrI_3 heterostructures the valley splitting shows an unprecedented high tunability upon twisting and gating, ranging from 0 to 12 meV, equivalent to external magnetic fields of up to 60 T. Our results also stress the importance of documenting the twist angle when employing magnetic vdW heterostructures in experiments.

ACKNOWLEDGMENTS

This work was funded by the Deutsche Forschungsgemeinschaft (DFG, German Research Foundation) SFB 1277 (Project No. 314695032), SPP 2244 (Project No. 443416183), and the European Union Horizon 2020 Research and Innovation Program under Contract No. 881603 (Graphene Flagship).

[1] T. Vincent, J. Liang, S. Singh, E. G. Castanon, X. Zhang, A. McCreary, D. Jariwala, O. Kazakova, and Z. Y. Al Balushi, Opportunities in electrically tunable 2d materials beyond graphene: Recent progress and future outlook, Appl. Phys. Rev. **8**, 041320 (2021).

[2] Q. Ma, G. Ren, K. Xu, and J. Z. Ou, Tunable optical properties of 2d materials and their applications, Adv. Opt. Mater. **9**, 2001313 (2021).

[3] B. Dieny, I. L. Prejbeanu, K. Garello, P. Gambardella, P. Freitas, R. Lehndorff, W. Raberg, U. Ebels, S. O Demokritov, J. Akerman *et al.*, Opportunities and challenges for spintronics in the microelectronics industry, Nat. Electron. **3**, 446 (2020).

[4] H. Qiao, H. Liu, Z. Huang, R. Hu, Q. Ma, J. Zhong, and X. Qi, Tunable electronic and optical properties of 2d monoelemental materials beyond graphene for promising applications, Energy & Environmental Materials **4**, 522 (2021).

[5] J. F Sierra, J. Fabian, R. K Kawakami, S. Roche, and S. O Valenzuela, Van der waals heterostructures for spintronics and opto-spintronics, Nat. Nanotechnol. **16**, 856 (2021).

[6] S. Roche, J. Åkerman, B. Beschoten, J.-C. Charlier, M. Chshiev, S. Prasad Dash, B. Dlubak, J. Fabian, A. Fert, M. Guimarães, F. Guinea, I. Grigorieva, C. Schönenberger, P. Seneor, C. Stampfer, S. O. Valenzuela, X. Waintal, and B. van Wees, Graphene spintronics: The European Flagship perspective, 2D Mater. **2**, 030202 (2015).

[7] J. R. Schaibley, H. Yu, G. Clark, P. Rivera, J. S. Ross, K. L. Seyler, W. Yao, and X. Xu, Valleytronics in 2D materials, Nat. Rev. Mater. **1**, 16055 (2016).

[8] F. Wang, T. A. Shifa, P. Yu, P. He, Y. Liu, F. Wang, Z. Wang, X. Zhan, X. Lou, F. Xia, and J. He, New frontiers on van der waals layered metal phosphorous trichalcogenides, Adv. Funct. Mater. **28**, 1802151 (2018).

[9] N. Briggs, S. Subramanian, Z. Lin, X. Li, X. Zhang, K. Zhang, K. Xiao, D. Geohegan, R. Wallace, L.-Q. Chen, M. Terrones, A. Ebrahimi, S. Das, J. Redwing, C. Hinkle, K. Momeni, A. van Duin, V. Crespi, S. Kar, and J. A Robinson, A roadmap for electronic grade 2D materials, 2D Mater. **6**, 022001 (2019).

[10] K. Khan, A. K. Tareen, M. Aslam, R. Wang, Y. Zhang, A. Mahmood, Z. Ouyang, H. Zhang, and Z. Guo, Recent developments in emerging two-dimensional materials and their applications, J. Mater. Chem. C **8**, 387 (2020).

[11] Q. H. Wang, A. Bedoya-Pinto, M. Blei, A. H. Dismukes, A. Hamo, S. Jenkins, M. Koperski, Y. Liu, Q.-C. Sun, E. J. Telford *et al.*, The magnetic genome of two-dimensional van der waals materials, ACS Nano **16**, 6960 (2022).

[12] K.-Alexander N Duerloo, Y. Li, and E. J Reed, Structural phase transitions in two-dimensional mo-and w-dichalcogenide monolayers, Nat. Commun. **5**, 4214 (2014).

[13] S. Song, D. H. Keum, S. Cho, D. Perello, Y. Kim, and Y. H. Lee, Room temperature semiconductor–metal transition of

$MoTe_2$ thin films engineered by strain, Nano Lett. **16**, 188 (2016).

[14] W. Hou, A. Azizimanesh, A. Sewaket, T. Peña, C. Watson, M. Liu, H. Askari, and S. M Wu, Strain-based room-temperature non-volatile $MoTe_2$ ferroelectric phase change transistor, Nat. Nanotechnol. **14**, 668 (2019).

[15] J. Ye, Y. J Zhang, R. Akashi, Ms. S. Bahramy, R. Arita, and Y. Iwasa, Superconducting dome in a gate-tuned band insulator, Science **338**, 1193 (2012).

[16] F. Zhang, H. Zhang, S. Krylyuk, C. A Milligan, Y. Zhu, D. Y Zemlyanov, L. A Bendersky, B. P Burton, A. V Davydov, and J. Appenzeller, Electric-field induced structural transition in vertical $MoTe_2$- and $Mo_{1-x}W_xTe_2$-based resistive memories, Nat. Mater. **18**, 55 (2019).

[17] X. Qian, J. Liu, L. Fu, and J. Li, Quantum spin hall effect in two-dimensional transition metal dichalcogenides, Science **346**, 1344 (2014).

[18] D. A. Rehn, Y. Li, E. Pop, and E. J. Reed, Theoretical potential for low energy consumption phase change memory utilizing electrostatically-induced structural phase transitions in 2d materials, npj Comput. Mater. **4**, 2 (2018).

[19] Y. Li, Karel-Alexander N Duerloo, K. Wauson, and E. J. Reed, Structural semiconductor-to-semimetal phase transition in two-dimensional materials induced by electrostatic gating, Nat. Commun. **7**, 10671 (2016).

[20] W. Li, X. Qian, and J. Li, Phase transitions in 2d materials, Nat. Rev. Mater. **6**, 829 (2021).

[21] I. Žutić, A. Matos-Abiague, B. Scharf, H. Dery, and K. Belashchenko, Proximitized materials, Mater. Today **22**, 85 (2019).

[22] A. K. Geim and I. V. Grigorieva, Van der Waals heterostructures, Nature (London) **499**, 419 (2013).

[23] K. S. Novoselov, A. Mishchenko, A. Carvalho, and A. H. Castro Neto, 2D materials and van der Waals heterostructures, Science **353**, aac9439 (2016).

[24] M. Gmitra and J. Fabian, Graphene on transition-metal dichalcogenides: A platform for proximity spin-orbit physics and optospintronics, Phys. Rev. B **92**, 155403 (2015).

[25] M. Gmitra, D. Kochan, P. Högl, and J. Fabian, Trivial and inverted dirac bands and the emergence of quantum spin hall states in graphene on transition-metal dichalcogenides, Phys. Rev. B **93**, 155104 (2016).

[26] A. Avsar, J. Y. Tan, X. Luo, K. H. Khoo, Y. Yeo, K. Watanabe, T. Taniguchi, S. Y. Quek, and B. Özyilmaz, van der Waals bonded Co/h-BN contacts to ultrathin black phosphorus devices, Nano Lett. **17**, 5361 (2017).

[27] A Avsar, H Ochoa, F. Guinea, B Özyilmaz, B. van Wees, and I. J. Vera-Marun, Colloquium: Spintronics in graphene and other two-dimensional materials, Rev. Mod. Phys. **92**, 021003 (2020).

[28] M. Offidani, M. Milletari, R. Raimondi, and A. Ferreira, Optimal Charge-to-Spin Conversion in Graphene on Transition-Metal Dichalcogenides, Phys. Rev. Lett. **119**, 196801 (2017).

[29] T. S. Ghiasi, A. A. Kaverzin, P. J. Blah, and B. J. van Wees, Charge-to-Spin conversion by the Rashba–Edelstein Effect in two-dimensional van der waals heterostructures up to room temperature, Nano Lett. **19**, 5959 (2019).

[30] D. Khokhriakov, A. Md. Hoque, B. Karpiak, and S. P. Dash, Gate-tunable spin-galvanic effect in graphene-topological insulator van der waals heterostructures at room temperature, Nat. Commun. **11**, 3657 (2020).

[31] F. Herling, C. K. Safeer, J. Ingla-Aynés, N. Ontoso, L. E. Hueso, and F. Casanova, Gate tunability of highly efficient spin-to-charge conversion by spin hall effect in graphene proximitized with WSe_2, APL Mater. **8**, 071103 (2020).

[32] A. Kormányos, G. Burkard, M. Gmitra, J. Fabian, V. Zólyomi, N. D. Drummond, V. Fal'ko, and V. Fal'ko, K.P Theory for Two-dimensional transition metal dichalcogenide semiconductors, 2D Mater. **2**, 022001 (2014).

[33] G.-B. Liu, D. Xiao, Y. Yao, X. Xu, and W. Yao, Electronic structures and theoretical modelling of two-dimensional group-VIB transition metal dichalcogenides, Chem. Soc. Rev. **44**, 2643 (2015).

[34] P. Tonndorf, R. Schmidt, P. Böttger, X. Zhang, J. Börner, A. Liebig, M. Albrecht, C. Kloc, O. Gordan, Dietrich R. T. Zahn, S. Michaelis de Vasconcellos, and R. Bratschitsch, Photoluminescence emission and Raman response of monolayer MoS_2, $MoSe_2$, and WSe_2, Opt. Express **21**, 4908 (2013).

[35] S. Tongay, J. Zhou, C. Ataca, K. Lo, T. S. Matthews, J. Li, J. C. Grossman, and J. Wu, Thermally driven crossover from indirect toward direct bandgap in 2D Semiconductors: $MoSe_2$versus MoS_2, Nano Lett. **12**, 5576 (2012).

[36] G. Eda, H. Yamaguchi, D. Voiry, T. Fujita, M. Chen, and M. Chhowalla, Photoluminescence from chemically exfoliated MoS_2, Nano Lett. **11**, 5111 (2011).

[37] A Chaves, J. Azadani, H. Alsalman, D. Da Costa, R Frisenda, A. Chaves, S. H. Song, Y. Kim, D. He, J. Zhou *et al.*, Band-gap engineering of two-dimensional semiconductor materials, npj 2D Materials and Applications **4**, 29 (2020).

[38] R. Oliva, T. Wozniak, P. E. Faria Jr, F. Dybala, J. Kopaczek, J. Fabian, P. Scharoch, and R. Kudrawiec, Strong substrate strain effects in multilayered WS_2 revealed by high-pressure optical measurements, ACS Appl. Mater. Interfaces **14**, 19857 (2022).

[39] K. Zollner, Paulo E. Faria Junior, and J. Fabian, Strain-tunable orbital, spin-orbit, and optical properties of monolayer transition-metal dichalcogenides, Phys. Rev. B **100**, 195126 (2019).

[40] E. Blundo, M. Felici, T. Yildirim, G. Pettinari, D. Tedeschi, A. Miriametro, B. Liu, W. Ma, Y. Lu, and A. Polimeni, Evidence of the direct-to-indirect band gap transition in strained two-dimensional Ws_2, MoS_2, and WSe_2, Phys. Rev. Res. **2**, 012024(R) (2020).

[41] E. Blundo, E. Cappelluti, M. Felici, G. Pettinari, and A. Polimeni, Strain-tuning of the electronic, optical, and vibrational properties of two-dimensional crystals, Appl. Phys. Rev. **8**, 021318 (2021).

[42] D. Xiao, G.-B. Liu, W. Feng, X. Xu, and W. Yao, Coupled Spin and Valley Physics in Monolayers of MoS_2 and Other Group-VI Dichalcogenides, Phys. Rev. Lett. **108**, 196802 (2012).

[43] S. A. Vitale, D. Nezich, J. O. Varghese, P. Kim, N. Gedik, P. Jarillo-Herrero, D. Xiao, and M. Rothschild, Valleytronics: Opportunities, challenges, and paths forward, Small **14**, 1801483 (2018).

[44] Y. Liu, Y. Gao, S. Zhang, J. He, J. Yu, and Z. Liu, Valleytronics in transition metal dichalcogenides materials, Nano Res. **12**, 2695 (2019).

[45] H. Zeng, J. Dai, W. Yao, D. Xiao, and X. Cui, Valley polarization in MoS_2 monolayers by optical pumping, Nat. Nanotechnol. **7**, 490 (2012).

[46] K. F. Mak, K. He, J. Shan, and T. F Heinz, Control of valley polarization in monolayer MoS_2 by optical helicity, Nat. Nanotechnol. **7**, 494 (2012).

[47] F. Bussolotti, H. Kawai, Z. E. Ooi, V. Chellappan, D. Thian, A. Lin Christina Pang, and K. Eng Johnson Goh, Roadmap on finding chiral valleys: Screening 2D materials for valleytronics, Nano Futures **2**, 032001 (2018).

[48] F Langer, C. P. Schmid, S Schlauderer, M Gmitra, J Fabian, P. Nagler, C. Schüller, T Korn, P. G. Hawkins, J T Steiner, U Huttner, S. W. Koch, M Kira, and R Huber, Lightwave valleytronics in a monolayer of tungsten diselenide, Nature (London) **557**, 76 (2018).

[49] A. Srivastava, M. Sidler, A. V. Allain, D. S. Lembke, A. Kis, and A. Imamoglu, Valley Zeeman effect in elementary optical excitations of monolayer WSe_2, Nat. Phys. **11**, 141 (2015).

[50] G. Aivazian, Z. Gong, A. M. Jones, R. L. Chu, J. Yan, D. G. Mandrus, C. Zhang, D. Cobden, W. Yao, and X. Xu, Magnetic control of valley pseudospin in monolayer WSe_2, Nat. Phys. **11**, 148 (2015).

[51] Y. Li, J. Ludwig, T. Low, A. Chernikov, X. Cui, G. Arefe, Y. D. Kim, A. M. van der Zande, A. Rigosi, H. M. Hill, S. H. Kim, J. Hone, Z. Li, D. Smirnov, and T. F. Heinz, Valley Splitting and Polarization by the Zeeman Effect in Monolayer $MoSe_2$, Phys. Rev. Lett. **113**, 266804 (2014).

[52] D. MacNeill, C. Heikes, K. F. Mak, Z. Anderson, A. Kormányos, V. Zólyomi, J. Park, and D. C. Ralph, Breaking of Valley Degeneracy by Magnetic Field in Monolayer $MoSe_2$, Phys. Rev. Lett. **114**, 037401 (2015).

[53] A. A. Mitioglu, P. Plochocka, Á. G. del Aguila, P. C. M. Christianen, G. Deligeorgis, S. Anghel, L. Kulyuk, and D. K. Maude, Optical investigation of monolayer and bulk tungsten diselenide (WSe_2) in high magnetic fields, Nano Lett. **15**, 4387 (2015).

[54] A. V. Stier, K. M. McCreary, B. T. Jonker, J. Kono, and S. A. Crooker, Exciton diamagnetic shifts and valley zeeman effects in monolayer WS_2 and MoS_2 to 65 tesla, Nat. Commun. **7**, 10643 (2016).

[55] T. Woźniak, P. E. Faria Junior, G. Seifert, A. Chaves, and J. Kunstmann, Exciton g factors of van der waals heterostructures from first-principles calculations, Phys. Rev. B **101**, 235408 (2020).

[56] P. E. F. Junior, K. Zollner, T. Woźniak, M. Kurpas, M. Gmitra, and J. Fabian, First-principles insights into the spin-valley physics of strained transition metal dichalcogenides monolayers, New J. Phys. **24**, 083004 (2022).

[57] Y. Ye, J. Xiao, H. Wang, Z. Ye, H. Zhu, M. Zhao, Y. Wang, J. Zhao, X. Yin, and X. Zhang, Electrical generation and control of the valley carriers in a monolayer transition metal dichalcogenide, Nat. Nanotechnol. **11**, 598 (2016).

[58] D. Zhong, K. L. Seyler, X. Linpeng, R. Cheng, N. Sivadas, B. Huang, E. Schmidgall, T. Taniguchi, K. Watanabe, M. A. McGuire, W. Yao, D. Xiao, K.-M. C. Fu, and X. Xu, Van der Waals engineering of ferromagnetic semiconductor heterostructures for spin and valleytronics, Sci. Adv. **3**, e1603113 (2017).

[59] Y. Ji, Y. Song, J. Zou, and W. Mi, Spin splitting and p-/n-type doping of two-dimensional $WSe_2/BiIrO_3$ (111) heterostructures, Phys. Chem. Chem. Phys. **20**, 6100 (2018).

[60] N. Li, J. Zhang, Y. Xue, T. Zhou, and Z. Yang, Large valley polarization in monolayer $MoTe_2$ on a magnetic substrate, Phys. Chem. Chem. Phys. **20**, 3805 (2018).

[61] J. Qi, X. Li, Q. Niu, and J. Feng, Giant and tunable valley degeneracy splitting in $MoTe_2$, Phys. Rev. B **92**, 121403(R) (2015).

[62] Q. Zhang, S. A. Yang, W. Mi, Y. Cheng, and U. Schwingenschlögl, Large spin-valley polarization in monolayer $MoTe_2$ on Top of EuO(111), Adv. Mater. **28**, 959 (2016).

[63] L. Xu, M. Yang, L. Shen, J. Zhou, T. Zhu, and Y. P. Feng, Large valley splitting in monolayer $\mathbf{WS_2}$ by proximity coupling to an insulating antiferromagnetic substrate, Phys. Rev. B **97**, 041405(R) (2018).

[64] C. Zhao, T. Norden, P. Zhang, P. Zhao, Y. Cheng, F. Sun, J. P. Parry, P. Taheri, J. Wang, Y. Yang, T. Scrace, K. Kang, S. Yang, G. X. Miao, R. Sabirianov, G. Kioseoglou, W. Huang, A. Petrou, and H. Zeng, Enhanced valley splitting in monolayer WSe_2 due to magnetic exchange field, Nat. Nanotechnol. **12**, 757 (2017).

[65] K. L. Seyler, D. Zhong, B. Huang, X. Linpeng, N. P. Wilson, T. Taniguchi, K. Watanabe, W. Yao, D. Xiao, M. A. McGuire, K.-M. C. Fu, and X. Xu, Valley manipulation by optically tuning the magnetic proximity effect in WSe_2/CrI_3 heterostructures, Nano Lett. **18**, 3823 (2018).

[66] B. Peng, Q. Li, X. Liang, P. Song, J. Li, K. He, D. Fu, Y. Li, C. Shen, H. Wang, C. Wang, T. Liu, L. Zhang, H. Lu, X. Wang, J. Zhao, J. Xie, M. Wu, L. Bi, L. Deng *et al.*, Valley polarization of trions and magnetoresistance in heterostructures of MoS_2 and yttrium iron garnet, ACS Nano **11**, 12257 (2017).

[67] T. Norden, C. Zhao, P. Zhang, R. Sabirianov, A. Petrou, and H. Zeng, Giant valley splitting in monolayer WS_2 by magnetic proximity effect, Nat. Commun. **10**, 4163 (2019).

[68] L. Ciorciaro, M. Kroner, K. Watanabe, T. Taniguchi, and A. Imamoglu, Observation of Magnetic Proximity Effect using Resonant Optical Spectroscopy of an Electrically Tunable $MoSe_2/CrBr_3$ Heterostructure, Phys. Rev. Lett. **124**, 197401 (2020).

[69] X. Fang, B. Zhou, N. Sun, L. Fu, and X. Wang, Valley splitting and magnetic anisotropy in two-dimensional VI_3/MSe_2 (M = W, Mo) heterostructures, Phys. Chem. Chem. Phys. **24**, 4374 (2022).

[70] D. Zhong, K. L. Seyler, X. Linpeng, N. P. Wilson, T. Taniguchi, K. Watanabe, M. A. McGuire, K.-M. C. Fu, D. Xiao, W. Yao, and X. Xu, Layer-resolved magnetic proximity effect in van der Waals heterostructures, Nat. Nanotechnol. **15**, 187 (2020).

[71] Z. Zhang, X. Ni, H. Huang, L. Hu, and F. Liu, Valley splitting in the van der waals heterostructure WSe_2/CrI_3: The role of atom superposition, Phys. Rev. B **99**, 115441 (2019).

[72] K. Zollner, P. E. Faria Junior, and J. Fabian, Proximity exchange effects in $MoSe_2$ and WSe_2 heterostructures with CrI_3: Twist angle, layer, and gate dependence, Phys. Rev. B **100**, 085128 (2019).

[73] M. Dabrowski, S. Guo, M. Strungaru, P. S Keatley, F. Withers, E. J. Santos, and R. J Hicken, All-optical control of spin in a 2d van der waals magnet, Nat. Commun. **13**, 5976 (2022).

[74] J. Choi, C. Lane, J.-X. Zhu, and S. A Crooker, Asymmetric magnetic proximity interactions in $MoSe_2/CrBr_3$ van der waals heterostructures, Nat. Mater. (2022).

[75] Y. Cao, V. Fatemi, S. Fang, K. Watanabe, T. Taniguchi, E. Kaxiras, and P. Jarillo-Herrero, Unconventional superconductivity in magic-angle graphene superlattices, Nature (London) **556**, 43 (2018).

[76] Y. Cao, V. Fatemi, A. Demir, S. Fang, S. L. Tomarken, J. Y. Luo, J. D. Sanchez-Yamagishi, K. Watanabe, T. Taniguchi, E. Kaxiras, R. C. Ashoori, and P. Jarillo-Herrero, Correlated insulator behaviour at half-filling in magic-angle graphene superlattices, Nature (London) **556**, 80 (2018).

[77] H. S. Arora, R. Polski, Y. Zhang, A. Thomson, Y. Choi, H. Kim, Z. Lin, I. Z. Wilson, X. Xu, J.-H. Chu *et al.*, Superconductivity in metallic twisted bilayer graphene stabilized by wse 2, Nature (London) **583**, 379 (2020).

[78] P. Stepanov, I. Das, X. Lu, A. Fahimniya, K. Watanabe, T. Taniguchi, F. H. Koppens, J. Lischner, L. Levitov, and D. K. Efetov, Untying the insulating and superconducting orders in magic-angle graphene, Nature (London) **583**, 375 (2020).

[79] X. Lu, P. Stepanov, W. Yang, M. Xie, M. A. Aamir, I. Das, C. Urgell, K. Watanabe, T. Taniguchi, G. Zhang *et al.*, Superconductors, orbital magnets and correlated states in magic-angle bilayer graphene, Nature (London) **574**, 653 (2019).

[80] A. L. Sharpe, E. J. Fox, A. W. Barnard, J. Finney, K. Watanabe, T. Taniguchi, M. A. Kastner, and D. Goldhaber-Gordon, Emergent ferromagnetism near three-quarters filling in twisted bilayer graphene, Science **365**, 605 (2019).

[81] Y. Saito, F. Yang, J. Ge, X. Liu, T. Taniguchi, K. Watanabe, J. Li, E. Berg, and A. F. Young, Isospin pomeranchuk effect in twisted bilayer graphene, Nature (London) **592**, 220 (2021).

[82] M. Serlin, C. L. Tschirhart, H. Polshyn, Y. Zhang, J. Zhu, K. Watanabe, T. Taniguchi, L. Balents, and A. F. Young, Intrinsic quantized anomalous hall effect in a moire heterostructure, Science **367**, 900 (2020).

[83] A. Nimbalkar and H. Kim, Opportunities and challenges in twisted bilayer graphene: A review, Nano-Micro Letters **12**, 126 (2020).

[84] N. Bultinck, S. Chatterjee, and M. P. Zaletel, Mechanism for Anomalous Hall Ferromagnetism in Twisted Bilayer Graphene, Phys. Rev. Lett. **124**, 166601 (2020).

[85] C. Repellin, Z. Dong, Y.-H. Zhang, and T. Senthil, Ferromagnetism in Narrow Bands of Moiré Superlattices, Phys. Rev. Lett. **124**, 187601 (2020).

[86] Y. Choi, J. Kemmer, Y. Peng, A. Thomson, H. Arora, R. Polski, Y. Zhang, H. Ren, J. Alicea, G. Refael *et al.*, Electronic correlations in twisted bilayer graphene near the magic angle, Nat. Phys. **15**, 1174 (2019).

[87] S. Lisi, X. Lu, T. Benschop, T. A. de Jong, P. Stepanov, J. R. Duran, F. Margot, I. Cucchi, E. Cappelli, A. Hunter *et al.*, Observation of flat bands in twisted bilayer graphene, Nat. Phys. **17**, 189 (2021).

[88] L. Balents, C. R. Dean, D. K. Efetov, and A. F. Young, Superconductivity and strong correlations in moiré flat bands, Nat. Phys. **16**, 725 (2020).

[89] T. M. R. Wolf, J. L. Lado, G. Blatter, and O. Zilberberg, Electrically Tunable Flat Bands and Magnetism in Twisted Bilayer Graphene, Phys. Rev. Lett. **123**, 096802 (2019).

[90] Z. Zhu, S. Carr, D. Massatt, M. Luskin, and E. Kaxiras, Twisted Trilayer Graphene: A Precisely Tunable Platform for Correlated Electrons, Phys. Rev. Lett. **125**, 116404 (2020).

[91] J. M. Park, Y. Cao, K. Watanabe, T. Taniguchi, and P. Jarillo-Herrero, Tunable strongly coupled superconductivity in magic-angle twisted trilayer graphene, Nature (London) **590**, 249 (2021).

[92] G. Chen, L. Jiang, S. Wu, B. Lyu, H. Li, B. L. Chittari, K. Watanabe, T. Taniguchi, Z. Shi, J. Jung *et al.*, Evidence of a gate-tunable mott insulator in a trilayer graphene moiré superlattice, Nat. Phys. **15**, 237 (2019).

[93] G. Chen, A. L. Sharpe, E. J. Fox, Y.-H. Zhang, S. Wang, L. Jiang, B. Lyu, H. Li, K. Watanabe, T. Taniguchi *et al.*, Tunable correlated chern insulator and ferromagnetism in a moiré superlattice, Nature (London) **579**, 56 (2020).

[94] G. Chen, A. L. Sharpe, P. Gallagher, I. T. Rosen, E. J. Fox, L. Jiang, B. Lyu, H. Li, K. Watanabe, T. Taniguchi *et al.*, Signatures of tunable superconductivity in a trilayer graphene moiré superlattice, Nature (London) **572**, 215 (2019).

[95] H. Zhou, T. Xie, A. Ghazaryan, T. Holder, J. R. Ehrets, E. M. Spanton, T. Taniguchi, K. Watanabe, E. Berg, M. Serbyn *et al.*, Half-and quarter-metals in rhombohedral trilayer graphene, Nature (London) **598**, 429 (2021).

[96] Y.-Z. Chou, F. Wu, J. D. Sau, and S. D. Sarma, Acoustic-Phonon-Mediated Superconductivity in Rhombohedral Trilayer Graphene, Phys. Rev. Lett. **127**, 187001 (2021).

[97] V. T. Phong, P. A. Pantaleón, T. Cea, and F. Guinea, Band structure and superconductivity in twisted trilayer graphene, Phys. Rev. B **104**, L121116 (2021).

[98] H. Zhou, T. Xie, T. Taniguchi, K. Watanabe, and A. F. Young, Superconductivity in rhombohedral trilayer graphene, Nature (London) **598**, 434 (2021).

[99] W. Qin and A. H. MacDonald, In-Plane Critical Magnetic Fields in Magic-Angle Twisted Trilayer Graphene, Phys. Rev. Lett. **127**, 097001 (2021).

[100] Y. Tang, L. Li, T. Li, Y. Xu, S. Liu, K. Barmak, K. Watanabe, T. Taniguchi, A. H. MacDonald, J. Shan *et al.*, Simulation of hubbard model physics in WSe_2/WS_2 moiré superlattices, Nature (London) **579**, 353 (2020).

[101] P. K. Barman, P. Upadhyay, R. Rajarapu, S. K. Yadav, L. KVP, and P. K. Nayak, Twist-dependent tuning of excitonic emissions in bilayer WSe_2, ACS Omega **7**, 6412 (2022).

[102] G. Yu, L. Wen, G. Luo, and Y. Wang, Band structures and topological properties of twisted bilayer $MoTe_2$ and WSe_2, Phys. Scr. **96**, 125874 (2021).

[103] Y. Xu, A. Ray, Y.-T. Shao, S. Jiang, K. Lee, D. Weber, J. E. Goldberger, K. Watanabe, T. Taniguchi, D. A. Muller *et al.*, Coexisting ferromagnetic–antiferromagnetic state in twisted bilayer CrI_3, Nat. Nanotechnol. **17**, 143 (2022).

[104] G. Cheng, M. M. Rahman, A. L. Allcca, A. Rustagi, X. Liu, L. Liu, L. Fu, Y. Zhu, Z. Mao, K. Watanabe, T. Taniguchi, P. Upadhyaya, and Y. P. Chen, Electrically tunable moiré magnetism in twisted double bilayer antiferromagnets, arXiv:2204.03837.

[105] S. Yan, S. Qi, D. Wang, and W. Mi, Novel electronic structures and magnetic properties in twisted two-dimensional graphene/janus 2h–vsete heterostructures, Phys. E **134**, 114854 (2021).

[106] A. David, P. Rakyta, A. Kormányos, and G. Burkard, Induced spin-orbit coupling in twisted graphene–transition metal dichalcogenide heterobilayers: Twistronics meets spintronics, Phys. Rev. B **100**, 085412 (2019).

[107] Y. Li and M. Koshino, Twist-angle dependence of the proximity spin-orbit coupling in graphene on transition-metal dichalcogenides, Phys. Rev. B **99**, 075438 (2019).

[108] T. Naimer, K. Zollner, M. Gmitra, and J. Fabian, Twist-angle dependent proximity induced spin-orbit coupling in graphene/transition metal dichalcogenide heterostructures, Phys. Rev. B **104**, 195156 (2021).

[109] A. Pezo, Z. Zanolli, N. Wittemeier, P. Ordejó n, A. Fazzio, S. Roche, and J. H. Garcia, Manipulation of spin transport in graphene/transition metal dichalcogenide heterobilayers upon twisting, 2D Mater. **9**, 015008 (2022).

[110] S. Lee, D. J. P. de Sousa, Y.-K. Kwon, F. de Juan, Z. Chi, F. Casanova, and T. Low, Charge-to-spin conversion in twisted graphene/WSe_2 heterostructures, Phys. Rev. B **106**, 165420 (2022).

[111] C. G. Péterfalvi, A. David, P. Rakyta, G. Burkard, and A. Kormányos, Quantum interference tuning of spin-orbit coupling in twisted van der waals trilayers, Phys. Rev. Res. **4**, L022049 (2022).

[112] A. Veneri, D. T. Perkins, C. G. Péterfalvi, and A. Ferreira, Twist-angle controlled collinear edelstein effect in van der waals heterostructures, Phys. Rev. B **106**, L081406 (2022).

[113] C. Ernandes, L. Khalil, H. Henck, M.-Q. Zhao, J. Chaste, F. Oehler, A. T. C. Johnson, M. C. Asensio, D. Pierucci, M. Pala, J. Avila, and A. Ouerghi, Strain and spin-orbit coupling engineering in twisted WS_2/graphene heterobilayer, Nanomaterials **11**, 2921 (2021).

[114] K. Zollner and J. Fabian, Engineering proximity exchange by twisting: Reversal of ferromagnetic and emergence of antiferromagnetic dirac bands in Graphene/$Cr_2Ge_2Te_6$, Phys. Rev. Lett. **128**, 106401 (2022).

[115] M. Ge, H. Wang, J. Wu, C. Si, J. Zhang, and S. Zhang, Enhanced valley splitting of WSe_2 in twisted van der waals WSe_2/CrI_3 heterostructures, npj Comput. Mater. **8**, 32 (2022).

[116] Z. Wu, J. Yu, and S. Yuan, Strain-tunable magnetic and electronic properties of monolayer CrI_3, Phys. Chem. Chem. Phys. **21**, 7750 (2019).

[117] G. Catarina, N. M. R. Peres, and J. Fernández-Rossier, Magneto-optical kerr effect in spin split two-dimensional massive dirac materials, 2D Mater. **7**, 025011 (2020).

[118] J. C. G. Henriques, G. Catarina, A. T. Costa, J. Fernández-Rossier, and N. M. R. Peres, Excitonic magneto-optical kerr effect in two-dimensional transition metal dichalcogenides induced by spin proximity, Phys. Rev. B **101**, 045408 (2020).

[119] B. Scharf, G. Xu, A. Matos-Abiague, and I. Žutić, Magnetic Proximity Effects in Transition-Metal Dichalcogenides: Converting Excitons, Phys. Rev. Lett. **119**, 127403 (2017).

[120] K. Zollner, P. E. Faria Junior, and J. Fabian, Giant proximity exchange and valley splitting in transition metal dichalcogenide/*h*BN/(Co, Ni) heterostructures, Phys. Rev. B **101**, 085112 (2020).

[121] S. R. Bahn and K. W. Jacobsen, An object-oriented scripting interface to a legacy electronic structure code, Comput. Sci. Eng. **4**, 56 (2002).

[122] P. Lazic, Cellmatch: Combining two unit cells into a common supercell with minimal strain, Comput. Phys. Commun. **197**, 324 (2015).

[123] D. S. Koda, F. Bechstedt, M. Marques, and L. K. Teles, Coincidence lattices of 2d crystals: Heterostructure predictions and applications, J. Phys. Chem. C **120**, 10895 (2016).

[124] S. Carr, S. Fang, and E. Kaxiras, Electronic-structure methods for twisted moiré layers, Nat. Rev. Mater. **5**, 748 (2020).

[125] M. A. McGuire, H. Dixit, V. R. Cooper, and B. C. Sales, Coupling of crystal structure and magnetism in the layered, ferromagnetic insulator CrI_3, Chem. Mater. **27**, 612 (2015).

[126] W. J. Schutte, J. L. De Boer, and F. Jellinek, Crystal structures of tungsten disulfide and diselenide, J. Solid State Chem. **70**, 207 (1987).

[127] P. B. James and M. T. Lavik, The crystal structure of MoSe2, Acta Crystallogr. **16**, 1183 (1963).

[128] See Supplemental Material at http://link.aps.org/supplemental/10.1103/PhysRevB.107.035112, including Refs. [[39,56,72,106,107],[114,116,125–127]], where we show all twisted heterostructure geometries and discuss about the origin of the reversal of the TMDC VB spin splitting. In addition, we list the model parameters for the electric field study, briefly address different stackings, the influence of strain, the twist angles between 30° to 60°, and show the calculated absorption spectra.

[129] P. Hohenberg and W. Kohn, Inhomogeneous electron gas, Phys. Rev. **136**, B864 (1964).

[130] P. Giannozzi, S. Baroni, N. Bonini, M. Calandra, R. Car, C. Cavazzoni, D. Ceresoli, G. L. Chiarotti, M. Cococcioni, I. Dabo, A. D. Corso, S. de Gironcoli, S. Fabris, G. Fratesi, R. Gebauer, U. Gerstmann, C. Gougoussis, A. Kokalj, M. Lazzeri, L. Martin-Samos *et al.*, QUANTUM ESPRESSO: A modular and open-source software project for quantum simulations of materials, J. Phys.: Condens. Matter **21**, 395502 (2009).

[131] P. Giannozzi, O. Andreussi, T. Brumme, O. Bunau, M. B. Nardelli, M. Calandra, R. Car, C. Cavazzoni, D. Ceresoli, M. Cococcioni, N. Colonna, I. Carnimeo, A. Dal Corso, S. de Gironcoli, P. Delugas, R. A. DiStasio, A. Ferretti, A. Floris, G. Fratesi, G. Fugallo *et al.*, Advanced capabilities for materials modelling with quantum ESPRESSO, J. Phys.: Condens. Matter **29**, 465901 (2017).

[132] X. Jiang, Q. Liu, J. Xing, N. Liu, Y. Guo, Z. Liu, and J. Zhao, Recent progress on 2d magnets: Fundamental mechanism, structural design and modification, Appl. Phys. Rev. **8**, 031305 (2021).

[133] G. Kresse and D. Joubert, From ultrasoft pseudopotentials to the projector augmented-wave method, Phys. Rev. B **59**, 1758 (1999).

[134] J. P. Perdew, K. Burke, and M. Ernzerhof, Generalized Gradient Approximation Made Simple, Phys. Rev. Lett. **77**, 3865 (1996).

[135] S. Grimme, Semiempirical gga-type density functional constructed with a long-range dispersion correction, J. Comput. Chem. **27**, 1787 (2006).

[136] S. Grimme, J. Antony, S. Ehrlich, and H. Krieg, A consistent and accurate *ab initio* parametrization of density functional dispersion correction (DFT-D) for the 94 elements H-Pu, J. Chem. Phys. **132**, 154104 (2010).

[137] V. Barone, M. Casarin, D. Forrer, M. Pavone, M. Sambi, and A. Vittadini, Role and effective treatment of dispersive forces in materials: Polyethylene and graphite crystals as test cases, J. Comput. Chem. **30**, 934 (2009).

[138] L. Bengtsson, Dipole correction for surface supercell calculations, Phys. Rev. B **59**, 12301 (1999).

[139] P. Jiang, L. Li, Z. Liao, Y. Zhao, and Z. Zhong, Spin direction controlled electronic band structure in two dimensional ferromagnetic CrI_3, Nano Lett. **18**, 3844 (2018).

[140] G. Balasubramanian, I. Y. Chan, R. Kolesov, M. Al-Hmoud, J. Tisler, C. Shin, C. Kim, A. Wojcik, P. R. Hemmer, A. Krueger *et al.*, Nanoscale imaging magnetometry with diamond spins under ambient conditions, Nature (London) **455**, 648 (2008).

[141] P. Wang, Z. Yuan, P. Huang, X. Rong, M. Wang, X. Xu, C. Duan, C. Ju, F. Shi, and J. Du, High-resolution vector microwave magnetometry based on solid-state spins in diamond, Nat. Commun. **6**, 6631 (2015).

[142] W. S. Huxter, M. L. Palm, M. L. Davis, P. Welter, C.-H. Lambert, M. Trassin, and C. L. Degen, Scanning gradiometry with a single spin quantum magnetometer, Nature Commun. **13**, 3761 (2022).

[143] T. C. Berkelbach, M. S. Hybertsen, and D. R. Reichman, Theory of neutral and charged excitons in monolayer transition metal dichalcogenides, Phys. Rev. B **88**, 045318 (2013).

[144] B. Huang, G. Clark, E. Navarro-Moratalla, D. R. Klein, R. Cheng, K. L. Seyler, D. Zhong, E. Schmidgall, M. A. McGuire, D. H. Cobden, W. Yao, D. Xiao, P. Jarillo-Herrero, and X. Xu, Layer-dependent ferromagnetism in a van der Waals crystal down to the monolayer limit, Nature (London) **546**, 270 (2017).

[145] R. Geick, C. H. Perry, and G. Rupprecht, Normal modes in hexagonal boron nitride, Phys. Rev. **146**, 543 (1966).

[146] A. V. Stier, N. P. Wilson, K. A. Velizhanin, J. Kono, X. Xu, and S. A. Crooker, Magnetooptics of Exciton Rydberg States in a Monolayer Semiconductor, Phys. Rev. Lett. **120**, 057405 (2018).

[147] M. Goryca, J. Li, A. V. Stier, T. Taniguchi, K. Watanabe, E. Courtade, S. Shree, C. Robert, B. Urbaszek, X. Marie, and S. A. Crooker, Revealing exciton masses and dielectric properties of monolayer semiconductors with high magnetic fields, Nat. Commun. **10**, 4172 (2019).